# Unconventional pairing symmetry of interacting Dirac fermions on a $\pi$-flux lattice

Huaiming Guo,[1,2] Ehsan Khatami,[3] Yao Wang,[4,5,6] Thomas P. Devereaux,[5,7] Rajiv R. P. Singh,[2] and Richard T. Scalettar[2]

[1]*Department of Physics, Key Laboratory of Micro-Nano Measurement-Manipulation and Physics (Ministry of Education), Beihang University, Beijing 100191, China*

[2]*Physics Department, University of California, Davis, California 95616, USA*

[3]*Department of Physics and Astronomy, San Jose State University, San Jose, California 95192, USA*

[4]*Department of Applied Physics, Stanford University, California 94305, USA*

[5]*SLAC National Accelerator Laboratory, Stanford Institute for Materials and Energy Sciences, 2575 Sand Hill Road, Menlo Park, California 94025, USA*

[6]*Department of Physics, Harvard University, Cambridge 02138, USA*

[7]*Geballe Laboratory for Advanced Materials, Departments of Physics and Applied Physics, Stanford University, Stanford, California 94305, USA*

(Received 24 August 2017; published 20 April 2018)

The pairing symmetry of interacting Dirac fermions on the $\pi$-flux lattice is studied with the determinant quantum Monte Carlo and numerical linked-cluster expansion methods. The $s^*$- (i.e., extended $s$-) and $d$-wave pairing symmetries, which are distinct in the conventional square lattice, are degenerate under the Landau gauge. We demonstrate that the dominant pairing channel at strong interactions is an unconventional $ds^*$-wave phase consisting of alternating stripes of $s^*$- and $d$-wave phases. A complementary mean-field analysis shows that while the $s^*$- and $d$-wave symmetries individually have nodes in the energy spectrum, the $ds^*$ channel is fully gapped. The results represent a new realization of pairing in Dirac systems, connected to the problem of chiral $d$-wave pairing on the honeycomb lattice, which might be more readily accessed by cold-atom experiments.

DOI: 10.1103/PhysRevB.97.155146

## I. INTRODUCTION

One of the dominant themes of condensed matter physics concerns unconventional superconductivity. Beginning with the heavy fermions and cuprates, where antiferromagnetic interactions are believed to mediate $d_{x^2-y^2}$-wave (for simplicity, referred to below as $d$-wave) pairing [1,2], to $s_\pm$ order in the iron pnictides [3,4], growing classes of materials including, for example, $Sr_2RuO_4$, $BC_3$, SrPtAs, $MoS_2$, and $Na_xCoO_2$ have been suggested to host pairing states in which there are additional broken parity, translation, time-reversal, and rotation symmetries.

One of the most well studied of these systems is doped graphene, where recent theoretical work has demonstrated a chiral $d$-wave superconducting state [5]. The qualitative explanation for this unconventional phase lies in the fact that the $d_{x^2-y^2}$ and $d_{xy}$ pairing symmetries belong to the same irreducible $E_{2g}$ representation of the honeycomb geometry, leading to the possibility that a complex combination might be energetically favored. However, determining the correct low-temperature superconducting symmetry, especially in competition with other types of spin density wave and charge density wave order, and the presence of significant electron correlation, requires the use of the most discerning analytic and numeric approaches. Indeed, methods ranging from mean-field theory [6,7] to functional renormalization group [8–11] and high-precision numerical simulations [12–16] have been applied to the problem.

The low-energy excitations in graphene are Dirac fermions, which possess a linear energy dispersion and density of states. In addition to the possibility of chiral $d$-wave pairing, these features lead to a variety of further unusual phenomena [17]. Given the tremendous interest in the emergent properties of Dirac fermions, it is natural to examine their behavior in the absence of graphene's sixfold rotational symmetry, and with different dispersion relations.

In this paper, we employ two unbiased numerical methods, the determinant quantum Monte Carlo (DQMC) [18] and the numerical linked-cluster expansion (NLCE) [19,20], to address this important issue by examining the pairing symmetry of the $\pi$-flux phase square lattice, which, like graphene, also hosts Dirac fermions. Originally proposed by Affleck and Marston to describe the pseudogap regime of the high-$T_c$ cuprates [21], the $\pi$-flux phase has recently been shown to be generated spontaneously with dynamical fermions coupled to a $\mathbb{Z}_2$ gauge theory in $(2+1)$ dimensions [22]. Our key findings are the following: (i) Our numerical results paint a consistent picture of the dominant pairing symmetry, which is found to be formed by pair creation with alternating stripes of extended $s$- (denoted as $s^*$-) and $d$-wave symmetries. (ii) This mixed structure originates in a symmetry linking the two pairing orders, and possesses a full gap, unlike the individual pieces. (iii) Superconductivity is most robust at intermediate values of the on-site repulsion $U$. (iv) Mean-field theory confirms the basic qualitative picture coming out of the DQMC/NLCE calculations. In the conclusions we will also address the possibility of engineering such lattices using optically trapped atomic systems.

## II. MODEL AND METHOD

We consider a Hubbard Hamiltonian describing interacting Dirac fermions in a $\pi$-flux model on a square lattice where

 

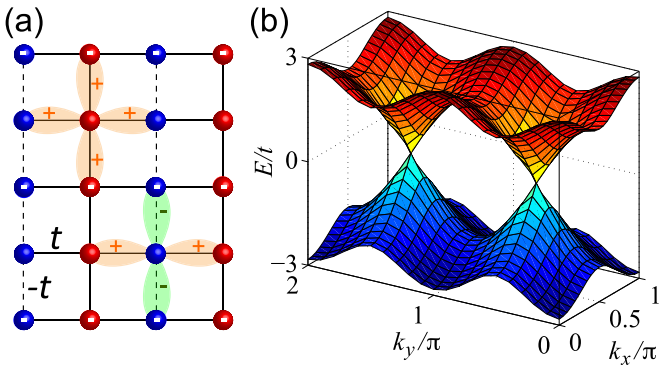


FIG. 1. (a) The $\pi$-flux lattice in the Landau gauge. The solid (dashed) lines represent positive (negative) hoppings. The $ds^*$-wave pairing symmetry is schematically shown. A gauge transformation on sites marked by the white bars shows that $s^*$ and $d$ waves are equivalent. (b) The noninteracting energy spectrum, which shows that the system is a semimetal with two inequivalent Dirac points. The corresponding density of state is linear for low energies and has a Van Hove singularity at $E/t = 2$.

each plaquette is threaded with half a flux quantum, [23,24] $\frac{1}{2}\Phi_0 = hc/(2e)$,

$$H = \sum_{\langle lj\rangle\sigma} t_{lj} e^{i\chi_{lj}} c^\dagger_{j\sigma} c_{l\sigma} + U \sum_i \left(n_{i\uparrow} - \frac{1}{2}\right)\left(n_{i\downarrow} - \frac{1}{2}\right), \quad (1)$$

where $c^\dagger_{j\sigma}$ and $c_{j\sigma}$ are the creation and annihilation operators, respectively, at site $j$ with spin $\sigma = \uparrow, \downarrow$. The hopping amplitudes between the nearest-neighbor sites $l$ and $j$ are $t_{lj} = t$, which we set to 1 as the unit of energy throughout our paper, and $\chi_{lj}$ is the Peierls phase arising from the magnetic flux $\chi_{lj} = \frac{2\pi}{\Phi_0}\int_{\mathbf{x}_l}^{\mathbf{x}_j} \mathbf{A}\cdot d\mathbf{x}$ with $\mathbf{A}$ the vector potential. In the Landau gauge we have $\mathbf{A} = \frac{1}{2}\Phi_0(0,x)$ and the Peierls phase is given by $\chi_{j,j+\hat{x}} = 0$, $\chi_{j,j+\hat{y}} = \pi j_x$. The resulting hopping pattern is shown in Fig. 1(a). The specific form of $\chi_{lj}$ is gauge dependent, allowing for different choices of the Peierls factors (see Appendix B). In the following, results are based on the geometry of Fig. 1(a). We have verified that results for other gauge choices are consistent.

The lattice in Fig. 1(a) has a two-site unit cell. In reciprocal space, with the reduced Brillouin zone ($|k_x| \leqslant \pi/2, |k_y| \leqslant \pi$), the Hamiltonian can be written as $H_0 = \sum_{\mathbf{k}\sigma} \psi^\dagger_{\mathbf{k}\sigma} \mathcal{H}_0(\mathbf{k}) \psi_{\mathbf{k}\sigma}$ with $\psi_{\mathbf{k}\sigma} = (c^1_{\mathbf{k}\sigma}, c^2_{\mathbf{k}\sigma})^T$ and $\mathcal{H}_0(\mathbf{k}) = 2t\cos k_x \sigma_x - 2t \cos k_y \sigma_z$, with $\sigma_{x,z}$ the Pauli matrices. The energy spectrum is given by $E_{\mathbf{k}} = \pm\sqrt{4t^2(\cos^2 k_x + \cos^2 k_y)}$. The noninteracting system is a semimetal with two inequivalent Dirac points at $\mathbf{K}_{1,2} = (\pi/2, \pm\pi/2)$ as shown in Fig. 1(b).

The interacting $\pi$-flux model is solved numerically by means of the DQMC and the NLCE methods. We also validate our results using exact diagonalization (ED) for a 4×4 lattice (see Appendix D). In DQMC, one decouples the on-site interaction term through the introduction of an auxiliary Hubbard-Stratonovich field, which is integrated out stochastically. The only errors are those associated with the statistical sampling, finite spatial lattice size, and the inverse temperature discretization. All are well controlled in the sense that they can be systematically reduced as needed, and further eliminated by appropriate extrapolations. At half-filling (average density of one fermion per site), we have access to low-temperature results, necessary to determine the pairing symmetry. Away from half-filling and in the presence of the sign problem [25,26] in the DQMC, we can access temperatures down to $T \sim 0.4$. The DQMC simulations are carried out on a 12×12 system, which is large enough to have negligible finite-size effects for the temperatures studied here (see Appendix C). Results represent averages of 10 independent runs with 10000 sweeps each.

In the NLCE, properties in the thermodynamic limit are expressed in terms of contributions from small clusters that can be embedded in the lattice. The latter are obtained via ED. We use a NLCE for the square lattice, modified to fit in the reduced symmetry of the $\pi$-flux model, and carry out the expansion up to the eighth order [20]. NLCE is error free in the temperature region of convergence and can be used to gauge systematic errors in DQMC in the common region of validity. Here we show both the bare results and those obtained after Euler resummation (see Appendix G).

The quantity on which we focus is the pairing structure factor, $S^\alpha(\mathbf{q}) = \sum_{\mathbf{r}} e^{i\mathbf{q}\cdot\mathbf{r}} P^\alpha(\mathbf{r})$, where $P^\alpha(\mathbf{r}_{ij}) = \langle \Delta^{\alpha\dagger}_i(0)\Delta^\alpha_j(0) + \Delta^\alpha_i(0)\Delta^{\alpha\dagger}_j(0)\rangle$ is the equal-time pair-pair correlation function. The general (time-dependent) pairing operator is defined as $\Delta^\alpha_i(\tau) = \sum_j f^\alpha_{ij} e^{\tau H} c_{i\uparrow} c_{j\downarrow} e^{-\tau H}$ with $f^\alpha_{ij} = \pm 1$ for the bond connecting $i$ and $j$, depending on the pairing symmetry $\alpha$. The $\Delta_{ds^*}$ operator, which proves to be dominant on the $\pi$-flux phase lattice, possesses $d$-wave phases ($f_{ij} = +1$ for $j = i \pm \hat{x}$ and $f_{ij} = -1$ for $j = i \pm \hat{y}$) for sites on vertical stripes of the lattice with $i_x$ odd, and $s^*$-wave symmetry ($f_{ij} = +1$ for both $j = i \pm \hat{x}$ and $j = i \pm \hat{y}$) for $i_x$ even. As we will show below, this symmetry has a larger superconducting response than more conventional singlet pairings in the $s^*$, $d_{x^2-y^2}$, $s_{xy}$, and $d_{xy}$ channels, and triplet pairings in $p_x$, $p_y$, and $p_{xy}$ channels [27].

Here we consider only the uniform pairing structure factor, $S^\alpha(\mathbf{q} = 0)$ and its correlated part, $S^\alpha_{\rm corr}$, obtained by subtracting off the uncorrelated parts from $S^\alpha$. One can also analyze the uniform pairing susceptibility,

$$\chi^\alpha(\mathbf{q} = 0) = \frac{1}{N}\int_0^\beta d\tau \sum_{ij} \left\langle \Delta^\alpha_i(\tau)\Delta^{\alpha\dagger}_j(0)\right\rangle, \quad (2)$$

which probes the decay of pairing correlations in the imaginary time as well as spatial directions. As with the structure factor, a subtraction of the uncorrelated pieces of $\chi^\alpha$ can be used to evaluate the pairing vertex [2]. Susceptibilities generally have stronger signals in ordered phases [28]. However, they also have larger error bars in the DQMC and are substantially more costly to compute.

## III. SUPERCONDUCTING PAIRING SYMMETRY

Spin fluctuations play an important role in pairing in Hamiltonians with repulsive electronic interactions, both competing with superconductivity at half-filling and providing the pairing glue upon doping. Unlike in the square lattice model with equal hoppings, for which the critical interaction $U_c = 0$, antiferromagnetic (AF) order in the $\pi$-flux lattice with Dirac fermions only develops above $U_c = 5.64 \pm 0.05$ [29–32]. However, we find that short-range AF correlations behave very similarly in

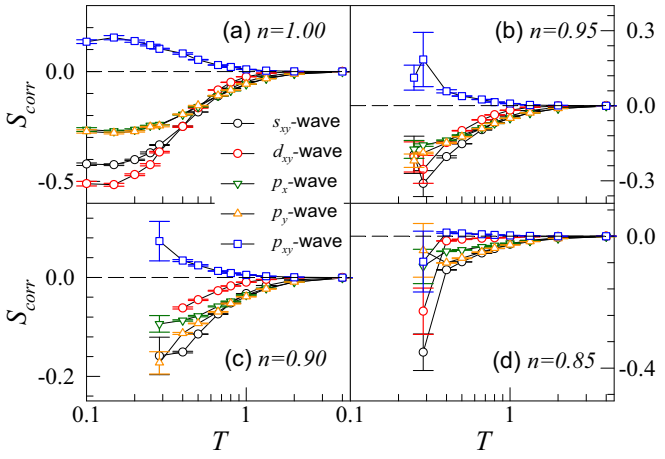


FIG. 2. DQMC results for the $\mathbf{q} = 0$ (uniform) $s_{xy}$-wave, $d_{xy}$-wave, $p_x$-wave, $p_y$-wave, and $p_{xy}$-wave pairing structure factors as a function of temperature. Here $U = 8t$ and the densities are: (a) $n = 1.00$; (b) $n = 0.95$; (c) $n = 0.90$; (d) $n = 0.85$. All channels are repulsive except for weakly attractive $p_{xy}$.

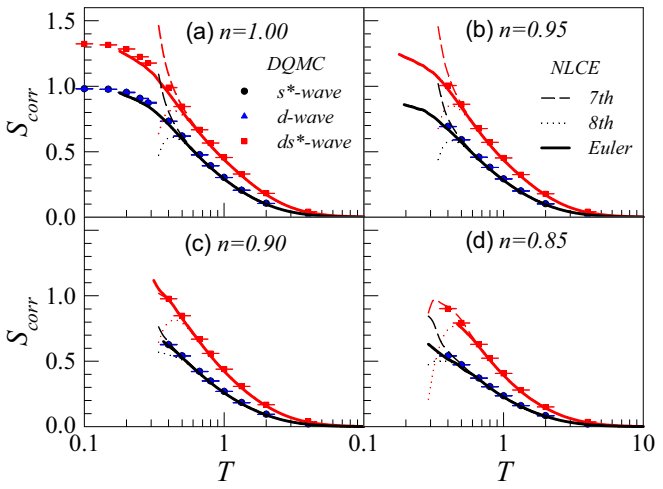


FIG. 3. The $ds^*$-wave, uniform $d$-wave, and $s^*$-wave pairing structure factors vs temperature for $U = 8t$ at densities $n = 1.00, 0.95, 0.90, 0.85$. $s^*$-wave and $d$-wave are identical to the accuracy of our calculations. Symbols are from the DQMC. Thin dashed and dotted lines are bare NLCE results for the seventh and eighth orders, respectively. Thick solid lines are results after the Euler resummation (see Appendix G).

the two models, suggesting that magnetic pairing mechanisms might be equally robust in the two cases (see Appendix E).

In Fig. 2, we show the correlated part of the uniform structure factor for several of the pairing symmetries, at various dopings for $U = 8$. DQMC can access low temperatures at half-filling, but is blocked by the sign problem in doped systems [25]. Nevertheless, the increasingly negative correlated structure factors in the $p_x, p_y, s_{xy}, d_{xy}$ modes offer compelling evidence that these symmetries are suppressed. For the $s_{xy}$ and $d_{xy}$ this can be understood as a consequence of the tendency towards AF order, with parallel spin fermions on next-nearest-neighbor (NNN) sites at odds with the presence of a singlet pair. The $p_{xy}$ mode is attractive, but its value is much smaller than $s^*$- and $d$-wave pairing (Fig. 3).

We find that $s^*$-, $d$-, and $ds^*$-wave pairings are an order of magnitude larger than $p_{xy}$-wave, and that $ds^*$-wave pairing is dominant in all parameter regions. By symmetry, $s^*$-, $d$-wave channels are equivalent in this model. This can be seen as follows: The $\pi$-flux lattice under Landau gauge belongs to the group $D_{2h}$. Among the irreducible representations for the group with $k_z = 0$, $A_{1g}$ has the basis function $k_x^2$ or $k_y^2$, which are independent. The $s^*$ ($d$) wave is a linear combination of the two basis functions $k_x^2 + k_y^2$ ($k_x^2 - k_y^2$); thus they are not necessarily equal from the point of view of the crystal symmetry group. However, gauge symmetry, a hidden symmetry underlying the Hamiltonian, enforces their equivalence. This can be directly seen by performing a transformation on the sites marked by white bars in Fig. 1(a), $c_{i,\sigma}(c_{i,\sigma}^\dagger) \to -c_{i,\sigma}(-c_{i,\sigma}^\dagger)$, under which the Hamiltonian remains unchanged while the uniform $s^*$-wave pairing becomes $d$-wave (or vice versa). This equivalence is confirmed within machine precision in the NLCE.

As shown in Fig. 3, the $ds^*$-wave pairing has the largest correlated structure factor for a range of dopings about half-filling. Results from NLCE and DQMC are in very good agreement and point to a saturation of $S_{\rm corr}$ at low temperatures at zero and 5% doping ($n = 0.95$). However, we are limited to relatively high temperatures at the other two doping values shown in Fig. 3, where $S_{\rm corr}$ continues to increase as $T$ is lowered. We focus on $n = 0.90$, and plot $S_{\rm corr}$ vs temperature for $U = 4, 6, 8$ and 12 in Fig. 4(a). At low temperature, the structure factor quickly rises as $U$ increases from $U = 4$, reaches a maximum in the intermediate-coupling region, and then slowly decreases. Figure 4(b) shows the susceptibility $\chi$ vs temperature for different interaction strengths at $n = 0.90$. For large $U$, there is a trend for the susceptibility to rapidly increase at low temperatures. The full $ds^*$-wave susceptibility shows a clear enhancement over its uncorrelated value, implying the pairing interaction is attractive. As in Fig. 3, the results from NLCE match well with DQMC in Fig. 4, indicating

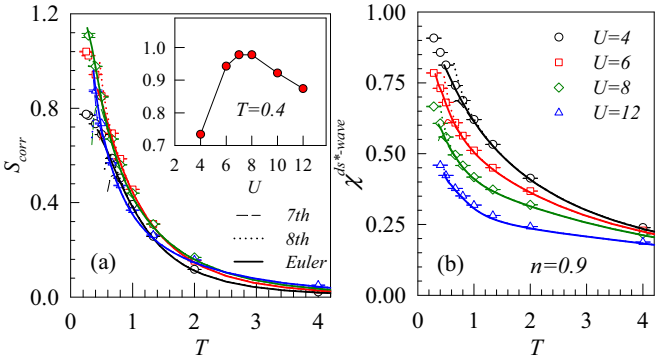


FIG. 4. (a) Temperature dependence of $ds^*$-wave pairing structure factor at density $n = 0.9$ for different values of the interaction. The inset shows the structure factor vs $U$ at a fixed temperature $T = 0.4$. A maximum is present at intermediate coupling. Symbols and lines in the main panels are the same as in Fig. 3. (b) The $ds^*$-wave pairing susceptibility as a function of the temperature at $n = 0.9$ for different values of $U$.

TABLE I. The character value λ of the gap matrix and $P_\alpha$ in Eq. (7) for three typical pairings.

| Pairing | λ | $P_\alpha$ |
|---|---|---|
| $s^*$ | $\lambda = \cos k_y \pm \lvert\cos k_x\rvert$ | $P_s^*(\mathbf{k}) = 2\Delta \cos k_y \tau_x \otimes I$ |
| $d$ | $\lambda = -\cos k_y \pm \lvert\cos k_x\rvert$ | $P_d(\mathbf{k}) = -2\Delta \cos k_y \tau_x \otimes I$ |
| $ds^*$ | $\lambda^2 = \cos k_x^2 + \cos k_y^2$ | $P_{ds^*}(\mathbf{k}) = 2\Delta \cos k_y \tau_x \otimes \sigma_z$ |

that systematic errors are not significant at the accessible temperatures.

Magnetic orders may compete with the superconductivity discussed above. We can not rule out the possibility of a magnetic ground state, however, lack of nesting, resulting in $U_c > 0$ for LRAFO, and the incommensurate filling make the magnetic order less competitive.

## IV. MEAN-FIELD DESCRIPTION OF THE SUPERCONDUCTING STATE

To study the physical properties of the possible superconducting states further, we analyze the gap function, $\Delta^\alpha = \sum_i \Delta_i^\alpha(0) = \sum_{\mathbf{k}} \Phi_\uparrow^T(\mathbf{k}) D^\alpha \Phi_\downarrow(-\mathbf{k})$, where

$$D^\alpha = \begin{pmatrix} \gamma \cos k_y & \cos k_x \\ \cos k_x & \beta \cos k_y \end{pmatrix}, \tag{3}$$

and $\Phi_\sigma(\mathbf{k}) = (c_{A,\mathbf{k}\sigma}, c_{B,\mathbf{k}\sigma})$ and $\gamma, \beta = 1(-1)$ for $s^*(d)$-wave pairing on each site. The character values λ of the gap matrix are shown in Table I. $s^*$ and $d$ waves have nodes along the blue lines in Fig. 5, while $ds^*$ wave is fully gapped.

A mean-field analysis of the superconducting spectrum provides a qualitative check on the DQMC and NLCE results reported above. The nonlocal pairing channels can not be decoupled from the on-site Hubbard term. However, at large $U$, the low-energy physics can be captured within the $t-J$ model [33]. The single-occupancy restriction is dealt with in an average way by the use of statistical weighting factors $t_{\text{eff}} = \frac{2\delta}{1+\delta} t$ and $J_{\text{eff}} = \frac{4}{(1+\delta)^2} J$ with $\delta$ the doping level and the coupling constant $J = \frac{4t^2}{U}$. The Heisenberg coupling is expressed in terms of the spin-singlet operator, $J_{\text{eff}}(\mathbf{S}_i \cdot \mathbf{S}_j - \frac{1}{4} n_i n_j) = -J_{\text{eff}} h_{ij}^\dagger h_{ij}$ with $h_{ij}^\dagger = \frac{1}{\sqrt{2}}(c_{i\uparrow}^\dagger c_{j\downarrow}^\dagger - c_{i\downarrow}^\dagger c_{j\uparrow}^\dagger)$, with $i$ and $j$ near neighbors.

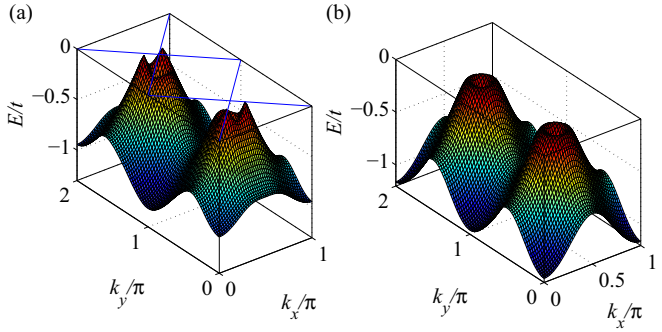


FIG. 5. The lower-energy dispersion within the mean-field theory near the Fermi energy for $s^*$ wave (or $d$ wave) (a) and $ds^*$ wave (b). Here the parameters are $\mu = 0.8, \Delta = 0.2$.

The mean-field parameter is $\Delta_{ij} = -J_{\text{eff}} \langle h_{ij} \rangle / \sqrt{2}$. In the basis $\psi_{\mathbf{k}} = (c_{1,\mathbf{k}\uparrow}, c_{2,\mathbf{k}\uparrow}, c_{1,-\mathbf{k}\downarrow}^\dagger, c_{2,-\mathbf{k}\downarrow}^\dagger)^T$, we arrive at the mean-field Hamiltonian: $H_{MF} = \sum_{\mathbf{k}} \psi_{\mathbf{k}}^\dagger \mathcal{H}_{MF}(\mathbf{k}) \psi_{\mathbf{k}} + E_0$ with $\mathcal{H}_{MF}(\mathbf{k}) = t \cos k_x \tau_z \otimes \sigma_x - t \cos k_y \tau_z \otimes \sigma_z - \frac{\mu}{2} \tau_z \otimes I + 2\Delta \cos k_x \tau_x \otimes \sigma_x + P_\alpha(\mathbf{k})$ and a constant term $E_0 = 4N \frac{\Delta^2}{J_{\text{eff}}}$. The ground state is then obtained by minimizing the free energy with respect to the order parameter Δ and doping $\delta$, which yields two self-consistent equations. After a numerical self-consistent iteration, we find that the order parameter Δ of the $ds^*$-wave pairing has larger values for the low doping levels, implying it is dominating in the ground state.

It is also straightforward to obtain the energy dispersion. We plot the bands near the Fermi energy in Fig. 5. The $s^*$- or $d$-wave pairing states are seen to have nodes, while the $ds^*$-wave state is fully gapped. A qualitative argument for the dominance of $ds^*$ pairing is the following: As emphasized by Scalapino [2], the presence of a self-consistent solution of the gap equation $\Delta_k = -\sum_{k'} \Gamma_{kk'} (\Delta_{k'}/2E_{k'}) \tanh(E_{k'}/2T)$, where $E_k$ is the superconducting quasiparticle dispersion, for repulsive interactions $\Gamma_{kk'}$ necessitates a change in sign of $\Delta_k$, and hence the presence of nodes. However, nodes reduce the overall energy lowering due to gap formation in the superconducting states. As a consequence, a symmetry, which enables a nontrivial self-consistent solution, while leaving the gap everywhere large, is energetically preferred.

## V. CONCLUSIONS

Pairing in the Hubbard model on a $\pi$-flux lattice was studied using exact/large-scale numerical methods. The $s^*$- and $d$-wave symmetries, which are distinct in the most commonly studied square lattice, are equivalent under the Landau gauge. Both DQMC and NLCE indicate that the dominating pairing channel at strong interactions is an unconventional $ds^*$ wave, for which the relative signs of the pairing amplitudes alternate between $d$-wave and $s^*$-wave patterns on adjacent stripes of the lattice. Within a mean-field analysis, the $s^*$- or $d$-wave channels can be shown individually to have nodes while the $ds^*$ channel is fully gapped. The results represent a profound extension of studies of interacting Dirac fermions in graphene by eliminating the specific symmetries of the honeycomb lattice. The DQMC studies reported here cannot access the Van Hove singularity at quarter-filling ($n = 0.5$), where the instability to a chiral $d$-wave state is especially prominent in graphene [5]. However, ED simulations on small lattices show a sign that the gapless $s^*$ or $d$ channel may dominate there, which warrants further studies.

Finally, we discuss how this phase might be accessed by state-of-the-art cold-atom experiments [34,35]. It is by now well established that Raman-assisted tunneling, and other methods, can be used to create effective magnetic fields on optical lattices [34–41], as well as more complex (non-Abelian) artificial gauge fields [42]. The hybridization pattern of Fig. 1 corresponds to alternating $\pm\pi$ magnetic flux on adjacent vertical stripes of the lattice, in precisely the geometry of Ref. [39], which achieved $\phi = \pm\pi/2$ flux, similarly alternating along the $\hat{x}$ direction. As discussed there, changing the wavelength of the

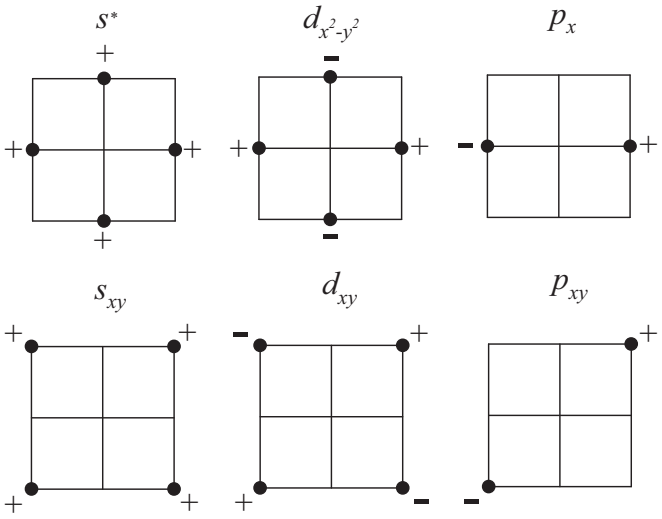


FIG. 6. Six of the nine the pairing symmetries available when the down spin fermion is created on a 3×3 lattice about the location of the up spin fermion at the center. On-site $s$ wave, where the down spin fermion is created at the same point as the up spin fermion, is not shown, nor are $p_y$ and $p_{yx}$, which are just 90° rotations of the $p_x$ and $p_{xy}$ symmetries illustrated in the two right-hand panels.

Raman lasers, or the angle between them, allows for generally tunable $\phi$. The pattern proposed here has already been realized for bosons [43]. Recent advances in high-resolution control of the confining potential, resulting in flat regions [44], can mitigate issues related to density inhomogeneity. These could, then, provide a precise and well-controlled realization of the unconventional $ds^*$ pairing symmetry described here.

## ACKNOWLEDGMENTS

The authors thank C. C. Chang, Z. X. Li, W. Pickett, S. Raghu, and F. Zhang for helpful discussions. H.G. acknowledges support from China Scholarship Council and NSFC under Grant No. 11774019. E.K. is supported by NSF under Grant No. DMR-1609560. Y.W. and T.P.D. are supported by DOE Grant No. DE-AC02-76SF00515. A portion of the computational work was performed using the resources of the National Energy Research Scientific Computing Center supported by DOE Grant No. DE-AC02-05CH11231. R.R.P.S. is supported by NSF under Grant No. DMR-1306048. The work of R.T.S. is supported by DOE Grant No. DE-SC0014671.

## APPENDIX A: CONTEXT OF PAIRING SYMMETRY

In early studies of the Hubbard Hamiltonian on a square lattice with uniform hopping (no flux), the amplitudes of the pairing responses of different symmetries were compared [1]. Figure 6 shows the real-space arrangements of the wave function of the down spin fermion around the up spin fermion. These correspond to momentum space pair creation operators,

$$\Delta_{\mathbf{k}}^{\alpha\dagger} = \sum_{\mathbf{k}} f_{\mathbf{k}}(\alpha)\, c_{\mathbf{k}\uparrow}^{\dagger} c_{-\mathbf{k}\downarrow}^{\dagger}, \tag{A1}$$

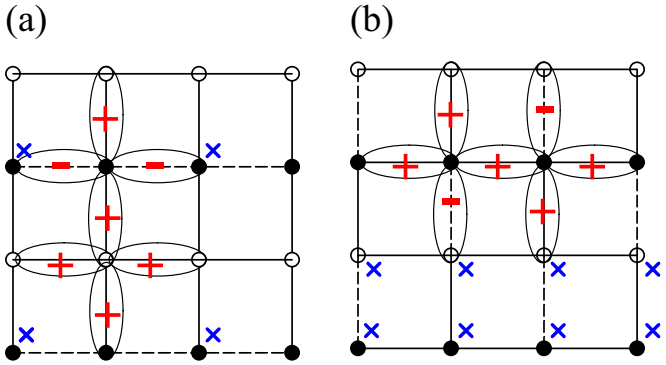


FIG. 7. The $\pi$-flux lattice under other gauges. The corresponding $ds^*$-wave pairing symmetry is schematically shown. The lattice and the pairing symmetry is transformed from the one under Landau gauge [see Fig. 1(a) in the main text] by a gauge transformation $c_{i,\sigma}(c_{i,\sigma}^{\dagger}) \rightarrow -c_{i,\sigma}(-c_{i,\sigma}^{\dagger})$ on the sites marked by blue crosses.

where $\alpha$ distinguishes the different symmetries,

$$\begin{aligned} f_{\mathbf{k}}(s) &= 1 \quad f_{\mathbf{k}}(s^*) = \cos k_x + \cos k_y \\ f_{\mathbf{k}}(p_x) &= \sin k_x \quad f_{\mathbf{k}}(d_{x^2-y^2}) = \cos k_x - \cos k_y \\ f_{\mathbf{k}}(p_y) &= \sin k_y \quad f_{\mathbf{k}}(d_{xy}) = \sin k_x \sin k_y \\ f_{\mathbf{k}}(s_{xy}) &= \cos k_x \cos k_y \quad f_{\mathbf{k}}(p_{xy}) = \sin (k_x + k_y) \\ f_{\mathbf{k}}(p_{yx}) &= \sin (k_x - k_y). \end{aligned} \tag{A2}$$

The $\pi$-flux lattice we consider here, which breaks translational symmetry in the $\hat{x}$ direction, allows for more complex symmetries, including the $ds^*$ arrangement of Fig. 1 of the main text. As illustrated there, the $ds^*$ symmetry alternates the $d_{x^2-y^2}$ and $s^*$ patterns of Fig. 6 as one moves between the $\pm\pi$ flux plaquettes.

## APPENDIX B: GAUGE SYMMETRY

The $\pi$-flux lattice can be realized with different choices of the hopping, i.e., with different gauges, as shown in Fig. 7. The hopping pattern is gauge dependent, but so are the phases of the $ds^*$ hopping. Two of the alternate choices are shown in Fig. 7. In Fig. 7(a), the vector potential $\mathbf{A} = -\frac{1}{2}\Phi_0(y,0)$ is chosen. As a check on our algorithm, we performed simulations of these transformed systems, and verified that all results are consistent with those in the main text.

## APPENDIX C: FINITE-SIZE EFFECTS

In the main text, all DQMC results were obtained on a 12×12 lattice. In Fig. 8, we show some results on 10×10 lattice to assess finite-size effects. The absolute values of the differences between the two sizes are of order $10^{-3}$. We conclude finite-size effects at the temperatures considered here are small. This fact is also implied by the agreement between the NLCE calculations shown in the main text, which represent the thermodynamic limit, yet match the DQMC results well.

We also note that on the 10×10 lattice, the Dirac points, which are located at $(\pi/2, \pm\pi/2)$, are not captured by the discrete momenta. As a consequence, the noninteracting band structure is not degenerate as is the case on 12×12 lattice. (In

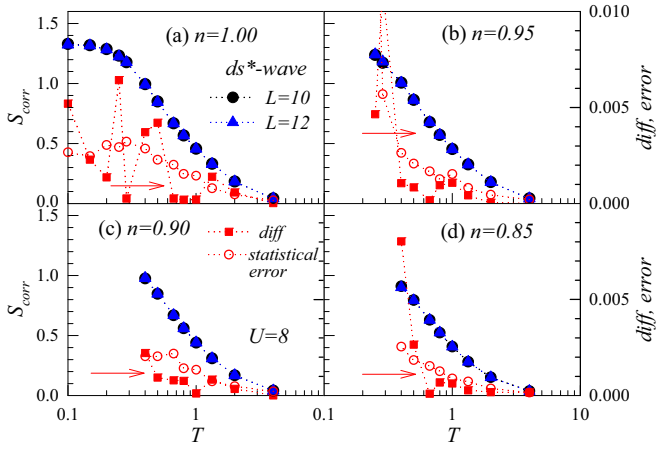


FIG. 8. The correlated pairing structure factors for two different lattice sizes, $L = 10$ (black circles) and $L = 12$ (blue triangles). The absolute difference for the densities $n = 1.00, 0.95, 0.90, 0.85$ at $U = 8$ is of order $10^{-3}$, which is comparable to the statistical error bars (the corresponding axis is marked by the red arrow).

one dimension, at $U = 0$, the ground-state energy at half-filling of lattices of size $4n$ and $4n + 2$ approach the thermodynamic limit from opposite directions owing to the presence/absence of $k$ points at the Fermi surface). Thus the agreement between the $10\times10$ and $12\times12$ lattices is an even more strict validation that finite-size effects are under good control. In general, for Hubbard Hamiltonians without any threading flux, a good rule of thumb [45] is that shell effects associated with the discrete momentum grid tend to be noticeable only for $U/t \lesssim 2$ on lattices of the sites studied here. Above this value, the interaction sufficiently smears the finite momentum grid to eliminate size effects.

## APPENDIX D: EXACT DIAGONALIZATION BENCHMARKS

To benchmark our DQMC simulations, we compare the DQMC results with those from ED on small sizes. As shown in Fig. 9, the finite-temperature DQMC values for the pair structure factors of all the symmetries precisely approach ED values at zero temperature.

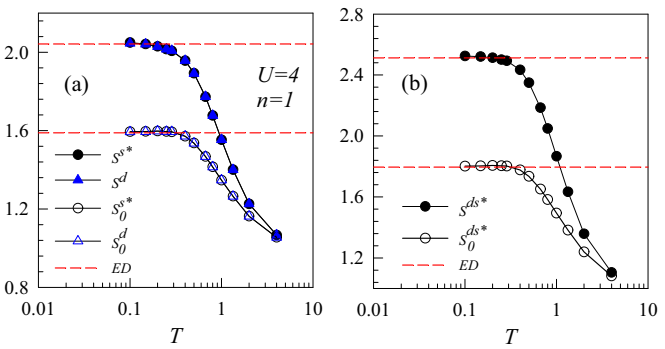


FIG. 9. The DQMC and ED results on $4\times4$ lattice for $n = 1$ and $U = 4$. The finite-temperature DQMC values tend to those of ED at zero temperature.

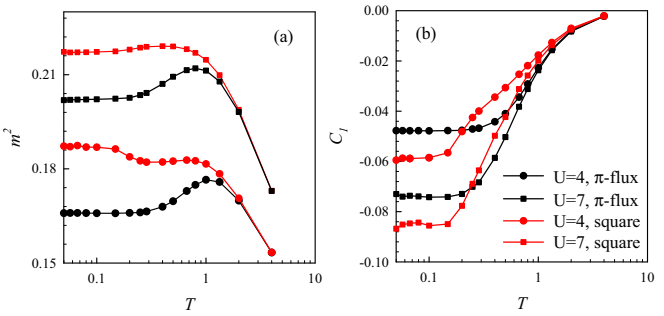


FIG. 10. The comparison of the local moment (a) and NN spin correlation (b) for fermions with linear and quadratic dispersions. The results are extrapolated to the continuous imaginary time limit using two separate simulations with $\Delta\tau = \frac{1}{16}$ and $\Delta\tau = \frac{1}{12}$.

## APPENDIX E: EFFECT OF FLUX ON LOCAL MAGNETIC CORRELATIONS

Figure 10 displays the local moment $m^2$ and NN spin-spin correlation function. $m^2$ is the zero separation ($\mathbf{l} = 0$) value of $C(\mathbf{l}) = \langle \frac{1}{2}(n_{\mathbf{j}+\mathbf{l}\uparrow} - n_{\mathbf{j}+\mathbf{l}\downarrow})\frac{1}{2}(n_{\mathbf{j}\uparrow} - n_{\mathbf{j}\downarrow})\rangle$ and reflects the degree of local charge fluctuations (double occupancy). $C(\mathbf{l})$ is rotationally invariant and in our simulations we average over all three directions to provide an improved estimator in DQMC simulations. As shown in Fig. 10(a), $m^2$ increases as $U$ is increased. Although the two cases $\phi = 0$ and $\phi = \pm\pi$, have nearly the same $m^2$ at high temperatures, this agreement breaks down at $T/t \lesssim 1$: Dirac fermions have smaller local moments at low temperatures compared to fermions with quadratic dispersion. For the NN spin correlation, at high temperatures the $\pi$-flux phase has bigger spin correlations, but there is a crossover so that at low $T$ the $\phi = 0$ lattice has larger $C_1 = C[\mathbf{l} = (1,0)]$.

## APPENDIX F: DIVERGENCE OF THE $DS^*$-WAVE PAIRING SUSCEPTIBILITY

At the superconducting transition temperature, the pairing susceptibility is expected to be divergent. Figure 11 plots $1/\chi$ as a function of the temperature at $n = 0.9$. The divergence

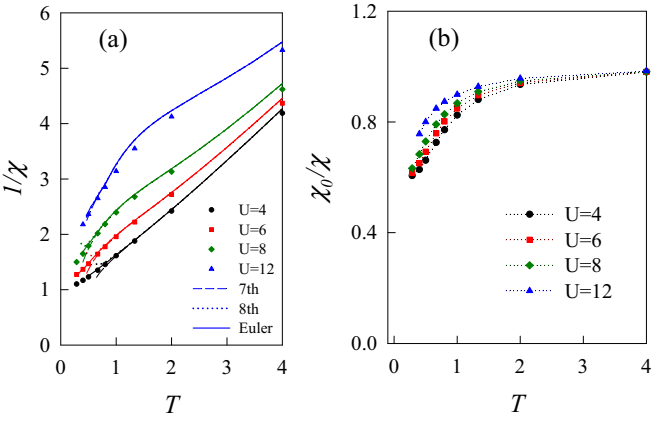


FIG. 11. (a) The inverse of the $ds^*$-wave pairing susceptibility as a function of the temperature at $n = 0.9$ for different values of $U$. (b) The inverse of the $ds^*$-wave pairing susceptibility divided by the local uncorrelated susceptibility at $r = 0$.

of $\chi$, especially at small $U$, is not completely compelling. However, as $U$ increases, the curves bend downward with growing slope and show an increasing tendency to cross zero at finite temperatures. To compare values of the susceptibilities for different $U$ on a more equal footing, we divide the $ds^*$-wave pairing susceptibility by the local uncorrelated susceptibility at $r = 0$. The scaled susceptibility dives more rapidly. Due to the small density at the Fermi surface for the situation we considered, it is expected that superconductivity may happen at low temperature, which is beyond the current capabilities of the DQMC and NLCE methods.

## APPENDIX G: NLCE RESUMMATION

Similar to the Pade approximations widely used in high-temperature series expansions, in the NLCE, one can take advantage of numerical resummation techniques, such as the Euler or Wynn methods [20,46], to extend the region of convergence to lower temperatures. Here we use the Euler resummation for the last five terms in the series. In this method, the original sum is replaced by

$$S_1 + S_2 + S_3 + \sum_{l=0}^{4} \frac{(-1)^l}{2^{l+1}} \Delta^l u_4, \tag{G1}$$

where $S_n$ is the $n$th term in the series, $u_n = (-1)^n S_n$, and $\Delta$ is defined as the forward differencing operator

$$\begin{aligned} \Delta^0 u_n &= u_n, \\ \Delta^1 u_n &= u_{n+1} - u_n, \\ \Delta^2 u_n &= u_{n+2} - 2u_{n+1} + u_n, \\ \Delta^3 u_n &= u_{n+3} - 3u_{n+2} + 3u_{n+1} - u_n, \\ &\vdots \end{aligned} \tag{G2}$$


[1] S. R. White, D. J. Scalapino, R. L. Sugar, N. E. Bickers, and R. T. Scalettar, Attractive and repulsive pairing interaction vertices for the two-dimensional Hubbard model, Phys. Rev. B **39**, 839 (1989).

[2] D. J. Scalapino, The case for $d_{x^2-y^2}$ pairing in the cuprate superconductors, Phys. Rep. **250**, 329 (1995).

[3] Q. Si, R. Yu, and E. Abrahams, High-temperature superconductivity in iron pnictides and chalcogenides, Nat. Rev. Mater. **1**, 16017 (2016).

[4] A. V. Chubukov, D. V. Efremov, and I. Eremin, Magnetism, superconductivity, and pairing symmetry in iron-based superconductors, Phys. Rev. B **78**, 134512 (2008).

[5] A. M. Black-Schaffer and C. Honerkamp, Chiral d-wave superconductivity in doped graphene, J. Phys.: Condens. Matter **26**, 423201 (2014).

[6] A. M. Black-Schaffer and S. Doniach, Resonating valence bonds and mean-field d-wave superconductivity in graphite, Phys. Rev. B **75**, 134512 (2007).

[7] W. Wu, M. M. Scherer, C. Honerkamp, and K. Le Hur, Correlated Dirac particles and superconductivity on the honeycomb lattice, Phys. Rev. B **87**, 094521 (2013).

[8] R. Nandkishore, L. S. Levitov, and A. V. Chubukov, Chiral superconductivity from repulsive interactions in doped graphene, Nat. Phys. **8**, 158 (2012).

[9] C. Honerkamp, Density Waves and Cooper Pairing on the Honeycomb Lattice, Phys. Rev. Lett. **100**, 146404 (2008).

[10] W. S. Wang, Y. Y. Xiang, Q. H. Wang, F. Wang, F. Yang, and D. H. Lee, Functional renormalization group and variational Monte Carlo studies of the electronic instabilities in graphene near 1/4 doping, Phys. Rev. B **85**, 035414 (2012).

[11] M. L. Kiesel, C. Platt, W. Hanke, D. A. Abanin, and R. Thomale, Competing many-body instabilities and unconventional superconductivity in graphene, Phys. Rev. B **86**, 020507 (2012).

[12] S. Pathak, V. B. Shenoy, and G. Baskaran, Possible high-temperature superconducting state with a $d + id$ pairing symmetry in doped graphene, Phys. Rev. B **81**, 085431 (2010).

[13] T. Ma, Z. Huang, F. Hu, and H. Lin, Pairing in graphene: A quantum Monte Carlo study., Phys. Rev. B **84**, 121410 (2011).

[14] Z. C. Gu, H. C. Jiang, D. N. Sheng, H. Yao, L. Balents, and X. G. Wen, Time-reversal symmetry breaking superconducting ground state in the doped Mott insulator on the honeycomb lattice, Phys. Rev. B **88**, 155112 (2013).

[15] S. Jiang, A. Mesaros, and Y. Ran, Chiral Spin-Density Wave, Spin-Charge-Chern Liquid, and $d + id$ Superconductivity in 1/4 -Doped Correlated Electronic Systems on the Honeycomb Lattice, Phys. Rev. X **4**, 031040 (2014).

[16] X. Y. Xu, S. Wessel, and Z. Y. Meng, Competing pairing channels in the doped honeycomb lattice Hubbard model, Phys. Rev. B **94**, 115105 (2016).

[17] A. K. Geim and K. S. Novoselov, The rise of graphene, Nat. Mater. **6**, 183 (2007).

[18] R. Blankenbecler, D. J. Scalapino, and R. L. Sugar, Monte Carlo calculations of coupled boson-fermion systems. I, Phys. Rev. D **24**, 2278 (1981).

[19] M. Rigol, T. Bryant, and R. R. P. Singh, Numerical Linked-Cluster Approach to Quantum Lattice Models, Phys. Rev. Lett. **97**, 187202 (2006).

[20] B. Tang, E. Khatami, and M. Rigol, A short introduction to numerical linked-cluster expansions, Comput. Phys. Commun. **184**, 557 (2013).

[21] I. Affleck and J. B. Marston, Large-n limit of the Heisenberg-Hubbard model: Implications for high-$T_c$ superconductors, Phys. Rev. B **37**, 3774 (1988).

[22] S. Gazit, M. Randeria, and A. Vishwanath, Emergent Dirac fermions and broken symmetries in confined and deconfined phases of Z2 gauge theories, Nat. Phys. **13**, 484 (2017).

[23] G. Rosenberg, B. Seradjeh, C. Weeks, and M. Franz, Creation and manipulation of anyons in a layered superconductor: Two-dimensional electron gas system, Phys. Rev. B **79**, 205102 (2009).

[24] Y. Jia, H. Guo, Z. Chen, S. Q. Shen, and S. Feng, Effect of interactions on two-dimensional Dirac fermions, Phys. Rev. B **88**, 075101 (2013).

[25] E. Y. Loh, J. E. Gubernatis, R. T. Scalettar, S. R. White, D. J. Scalapino, and R. L. Sugar, The sign problem in the numerical

simulation of many electron systems, Phys. Rev. B **41**, 9301 (1990).

[26] V. Iglovikov, E. Khatami, and R. T. Scalettar, Geometry dependence of the sign problem in quantum Monte Carlo simulations, Phys. Rev. B **92**, 045110 (2015)

[27] Here we only consider conventional pairings on square lattice. Though there are other possible ones (such as time-reversal breaking $d + is^*$, etc.), we find that $ds^*$ wave is the ground state of all allowed pairing symmetries. In our calculations, the pairing structure factor is formulated as $S = F^T M F$, with $M$ the paring matrix and $F$ the pairing wave. The eigenvector corresponding to the largest eigenvalue of $M$ is $d^*s$ wave.

[28] E. Khatami, R. T. Scalettar, and R. R. P. Singh, Finite-temperature superconducting correlations of the Hubbard model, Phys. Rev. B **91**, 241107 (2015).

[29] Y. Otsuka, S. Yunoki, and S. Sorella, Universal Quantum Criticality in the Metal-Insulator Transition of Two-Dimensional Interacting Dirac Electrons, Phys. Rev. X **6**, 011029 (2016).

[30] H. Yokoyama, S. Tamura S, and M. Ogata, Staggered flux state in two-dimensional Hubbard models, J. Phys. Soc. Japan **85**, 124707 (2016).

[31] C. C. Chang and R. T. Scalettar, Staggered-Flux Hubbard Model on a Square Lattice, Phys. Rev. Lett. **109**, 026404 (2012).

[32] F. P. Toldin, M. Hohenadler, F. F. Assaad, and I. F. Herbut, Fermionic quantum criticality in honeycomb and ¦Ðflux Hubbard models: Finite-size scaling of renormalization-group-invariant observables from quantum Monte Carlo, Phys. Rev. B **91**, 165108 (2015).

[33] F. C. Zhang and T. M. Rice, Effective Hamiltonian for the superconducting Cu oxides, Phys. Rev. B **37**, 3759 (1988).

[34] C. J. Kennedy, W. C. Burton, W. C. Chung, and W. Ketterle, Observation of Bose-Einstein condensation in a strong synthetic magnetic field, Nat. Phys. **11**, 859 (2015).

[35] N. Goldman, J. C. Budich, and P. Zoller, Topological quantum matter with ultracold gases in optical lattices, Nat. Phys. **12**, 639 (2016).

[36] D. Jaksch and P. Zoller, Creation of effective magnetic fields in optical lattices: the Hofstadter butterfly for cold neutral atoms, New J. Phys. **5**, 56 (2003).

[37] F. Gerbier and J. Dalibard, Gauge fields for ultracold atoms in optical superlattices, New J. Phys. **12**, 033007 (2010).

[38] E. J. Mueller, Artificial electromagnetism for neutral atoms: Escher staircase and Laughlin liquids, Phys. Rev. A **70**, 041603 (2004).

[39] M. Aidelsburger, M. Atala, S. Nascimbéne, S. Trotzky, Y. A. Chen, and I. Bloch, Experimental Realization of Strong Effective Magnetic Fields in an Optical Lattice, Phys. Rev. Lett. **107**, 255301 (2011).

[40] M. Aidelsburger, M. Atala, M. Lohse, J. T. Barreiro, B. Paredes, and I. Bloch, Realization of the Hofstadter Hamiltonian with Ultracold Atoms in Optical Lattices, Phys. Rev. Lett. **111**, 185301 (2013).

[41] H. Miyake, G. A. Siviloglou, C. J. Kennedy, W. C. Burton, and W. Ketterle, Realizing the Harper Hamiltonian with Laser-Assisted Tunneling in Optical Lattices, Phys. Rev. Lett. **111**, 185302 (2013).

[42] Y. J. Lin and I. B. Spielman, Synthetic gauge potentials for ultracold neutral atoms, J. Phys. B **49**, 183001 (2016), and references cited therein.

[43] M. E. Tai, A. Lukin, M. Rispoli, R. Schittko, T. Menke, D. Borgnia, P. M. Preiss, F. Grusdt, A. M. Kaufmanand, and M. Greiner, Microscopy of the interacting Harper-Hofstadter model in the two-body limit, Nature (London) **546**, 519 (2017)

[44] A. Mazurenko, C. S. Chiu, G. Ji, M. F. Parsons, M. Kanasz-Nagy, R. Schmidt, F. Grusdt, E. Demler, D. Greif, and M. Greiner, A cold-atom Fermi-Hubbard antiferromagnet, Nature (London) **545**, 462 (2017)

[45] C. N. Varney, C. R. Lee, Z. J. Bai, S. Chiesa, M. Jarrell, and R. T. Scalettar, Quantum Monte Carlo study of the two-dimensional fermion Hubbard model, Phys. Rev. B **80**, 075116 (2009).

[46] M. Rigol, T. Bryant, and R. R. P. Singh, Numerical linked-cluster algorithms. I. Spin systems on square, triangular, and kagome lattice, Phys. Rev. E **75**, 061118 (2007).